A simple model for daily basin-wide thermodynamic sea ice thickness growth retrieval

James Anheuser[1], Yinghui Liu[2], and Jeffrey R. Key[2]

[1]AOS UW-Madison, Madison, Wisconsin
[2]Center for Satellite Applications and Research, NOAA/NESDIS, Madison, Wisconsin

Correspondence: James Anheuser (anheuser@wisc.edu)

Abstract. As changes to Earth's polar climate accelerate, the need for robust, long–term sea ice thickness observation datasets for monitoring those changes and for verification of global climate models is clear. By linking a recently developed algorithm for retrieving snow–ice interface temperature from passive microwave satellite data to a thermodynamic sea ice energy balance relation known as Stefan's Law, we have developed a new retrieval method for estimating thermodynamic sea ice thickness growth from space: Stefan's Law Integrated Conducted Energy (SLICE). With an initial condition at the beginning of the sea ice growth season, the method can model basin-wide absolute sea ice thickness by combining the one-dimensional SLICE retrieval with an ice motion dataset. The advantages of the SLICE retrieval method include daily basin-wide coverage and a potential for use beginning in 1987. Validation of the retrieval against measurements from ten ice mass balance buoys show a mean correlation of 0.88 and a mean bias of 0.08 m over the course of an entire sea ice growth season. Despite its simplifications and assumptions relative to models like the Pan-Arctic Ice–Ocean Modeling and Assimilation System (PIOMAS), basin-wide SLICE performs equally to PIOMAS when compared against CryoSat-2 and Operation IceBridge.

1 Introduction

Observing sea ice concentration and areal extent from satellites is a well established practice (Liu et al., 2016; Meier et al., 2017; Markus and Cavalieri, 2000; Markus and Cavalieri, 2009; Comiso, 2009; Lavergne et al., 2019). There are methods based on data in the visual, infrared and microwave wavelength bands and climate data records produced from these methods are commonly cited as polar climate indicators (Stroeve et al., 2012; Screen and Simmonds, 2010; Liu et al., 2009).

While sea ice concentration is more readily observed, sea ice thickness provides a more complete characterization of the state of the climate system because it allows for calculation of sea ice volume and latent heat release. Recent literature has made clear that reliable long-term observations of basin wide sea ice thickness are needed in order to constrain the representations of sea ice in global climate models (Mayer et al., 2019). Sea ice thickness based observations of sea ice volume can be used along with other observations to refine the large range of projected sea ice area and volume across coupled global climate models (Docquier and Koenigk, 2021). Indeed, the lack of reliable long term sea ice thickness observation constraints is the primary barrier to reducing the uncertainty in future sea ice area and volume projections (Massonnet et al., 2018).

Sea ice thickness derived from space-based altimetry data collected by satellites like CryoSat-2 and ICESat-2 stand as the current state of the art (Connor et al., 2009; Kwok and Cunningham, 2008; Markus et al., 2017, Wingham et al., 2006; Laxon et al., 2013). Though the instruments aboard these satellites have relatively high spatial resolutions, it takes 28 days and 91 days, respectively, for CryoSat-2 and ICESat-2 to cover the entire Arctic due to their relatively low spatial coverage (Wang et al., 2016). Other strategies for retrieving sea ice thickness include a one-dimensional surface energy balance model driven by satellite products (Key et al., 2016) and estimating the thickness of thin sea ice using low-frequency passive microwave satellite data (Mecklenburg et al., 2012). A coupled ocean–sea ice model with assimilated observational data is also commonly referenced (Zhang and Rothrock, 2003). A newer approach involves correlating sea ice thickness with sea ice age (Liu et al., 2020). The various available products are discussed and compared against one another both qualitatively and quantitatively in Wang et al. (2016) and against upward looking sonar (ULS) in Sallila et al. (2019).

Recent efforts to retrieve temperature at the boundary between snow and sea ice, referred to as the snow–ice interface temperature, have opened a new door in polar climate observation (Lee and Sohn, 2015; Lee et al., 2018; Kilic et al., 2019). These methods take advantage of radiances from the Advanced Microwave Scanning Radiometer (AMSR)-Earth Observing System (-E), AMSR2, the Special Sensor for Microwave Imager (SSM/I) and Special Sensor Microwave Imager/Sounder (SSMIS) passive microwave instruments using channels whose wavelengths are not significantly absorbed by snow and therefore carry information from the snow–ice interface. Kang et al. (2021) demonstrated the utility of these snow–ice interface temperature data by using them to nudge a sea ice model, improving the model's results. By coupling this newly available snow–ice interface temperature data with Stefan's Law governing the thermodynamics of sea ice growth (Stefan, 1891; Lepparanta, 1993), we introduce a new method of retrieving thermodynamic sea ice thickness growth called Stefan's Law Integrated Conducted Energy (SLICE).

As sea ice accretes on the underside of the ice layer, the latent heat of fusion conducts up through the ice to the snow–ice interface. In Stefan's Law, that conducted heat and therefore rate of accretion is calculated using a heat conduction equation with the snow–ice interface temperature as the upper boundary condition and the local freezing temperature of sea water set as the lower boundary condition (Stefan, 1891; Lepparanta, 1993). By using the satellite retrieved snow–ice interface temperature in this relationship, SLICE is able to retrieve daily rate of ice accretion and model sea ice thickness on a basin-wide scale during the sea ice growth season by integrating these retrieved growth rates from an initial sea ice thickness condition. The methodology is applicable beginning in 1987 with the availability of the required passive microwave observations.

2 Data

The SLICE retrieval method described here utilizes passive microwave brightness temperatures and a passive microwave based sea ice concentration dataset. Modelling basin-wide sea ice thickness requires motion vectors and a satellite based initial condition. A preliminary validation of the retrieval method references sea ice thickness from ice mass balance buoy data, satellite and airborne altimeter based sea ice thickness data, and sea ice models.

2.1 Passive microwave brightness temperatures and sea ice concentration

The AMSR-E and AMSR2 brightness temperatures available from the National Snow and Ice Data Center (NSIDC) were used in this study (Cavalieri et al., 2014; Markus et al., 2018). The AMSR-E data is available for June 2002 through October 2011 and the AMSR2 data is available for July 2012 to the present. The AMSR2 data has been intercalibrated with the AMSR-E data and the brightness temperatures between these two instruments are treated here as a continuous dataset (Markus et al., 2018). The data is provided on a 25 km polar stereographic grid, but when needed on a basin-wide scale for use with the sea ice thickness retrieval method described here, the data were linearly interpolated to a 25 km Equal-Area Scalable Earth (EASE)-Grid 2.0.

The NASA Team 2 algorithm is a passive microwave brightness temperature sea ice concentration algorithm (Markus and Cavalieri, 2000). It as an enhancement to the original NASA Team algorithm (Cavalieri et al., 1984; Gloersen and Cavalieri, 1986) in that it adds 85 GHz frequency brightness temperatures to the original algorithm, which used only 19 GHz and 37 GHz data, in order to better account for interference from surface effects. The algorithm utilizes open ocean and 100% ice concentration tie points in polarization and spectral gradient ratios to determine sea ice concentration. While originally developed for use with SSM/I data (Markus and Cavalieri, 2000), the algorithm was planned to be and is now in use with AMSR-E and AMSR2 data. Here we use this AMSR-E and AMSR2 sea ice concentration data, which is available from the NSIDC as a part of the same dataset that contains the brightness temperatures used to calculate snow–ice interface temperature (Cavalieri et al., 2014; Markus et al., 2018).

2.2 Sea ice motion vectors

Sea ice is not static, but rather a dynamic collection of variably sized parcels that are each in constant horizontal motion under the effects of wind, ocean currents and internal stress. In order to treat sea ice in a lagrangian sense, the motion of these parcels must be understood. Here we use the Polar Pathfinder Daily 25 km EASE-Grid Sea Ice Motion Vectors, Version 4 available from the NSIDC (Tschudi et al., 2019; Tschudi et al., 2020). The product is available from 1978 to present at daily and weekly temporal resolution, each with basin-wide coverage and each on the 25 km EASE-Grid. Using an optimal interpolation scheme, ice motion vectors are created from cross correlated satellite brightness temperature data from AMSR-E, Advanced Very High Resolution Radiometer (AVHRR), Scanning Multichannel Microwave Radiometer (SMMR), SSM/I and SSMIS, along with International Arctic Buoy Program (IABP) buoy locations and a National Centers for Environmental Protection (NCEP)/ National Center for Atmospheric Research (NCAR) wind reanalysis data derived free drift estimate. Each satellite and buoy dataset are included in the optimal estimation scheme only when available within the life span of the ice motion product. This means input data sources vary throughout the record. DeRepentigny et al. (2016) found the weekly sea ice motion vectors to have a 7% median error when compared against IABP buoys between 1988 and 2011.

2.3 Airborne and satellite based sea ice thickness products

CryoSat-2 carries the SAR/Interferometric Radar Altimeter-2 (SIRAL-2) instrument (Wingham et al., 2006; Laxon et al., 2013) and was launched by the European Space Agency (ESA) in 2010. Similar to other satellite altimeters, ice thickness is determined from CryoSat-2 data by first calculating the thickness of the sea ice above sea level—known as the freeboard—by
90 determining the distance traveled by the radar signal between the satellite and the the ice surface and subtracting that distance from the satellite orbit altitude above sea level. An assumed snow loading provides a correction for the reduced propagation speed of the radar signal through snow. Then, the assumed snow loading and a hydrostatic balance is used to determine sea ice mass which in turn is converted to thickness using an assumed density (Laxon et al., 2013). Gridded ice thickness products derived from ESA CryoSat-2 Level 1b data are provided by the Centre for Polar Observation and Modelling (CPOM) (Tilling
95 et al., 2018), the National Aeronautics and Space Agency (NASA) Goddard Space Flight Center (GSFC) (Kurtz et al., 2014a), the Alfred Wegener Institute (Ricker et al., 2014; Hendricks and Ricker, 2020; Ricker et al., 2017a), the NASA Jet Propulsion Laboratory (Kwok and Cunningham, 2015), the ESA Climate Change Initiative (Hendricks et al., 2018) and the Laboratoire d'Études en Géophysique et Océanographie Spatiales Center for Topographic studies of the Ocean and Hydrosphere (Guerreiro et al., 2017). The primary differences between these datasets relate to averaging period, grid sizing and radar response waveform
100 retracking procedure.

The ESA Soil Moisture and Ocean Salinity (SMOS) satellite carries the Microwave Imaging Radiometer using Aperture Synthesis (MIRAS) instrument which measures 1.4 GHz passive microwave brightness temperatures at 35 to 50+ km resolution (Mecklenburg et al., 2012). While originally intended for measuring soil moisture and ocean salinity, the high penetration depth of the 1.4 GHz channel into sea ice allows for retrieval of an ice temperature that when incorporated into a radiative transfer
105 model yields a sea ice thickness estimate (Tian-Kunze et al., 2014). This approach has associated uncertainties in sea ice below 0.5 m thick that are lower than those of satellite altimeters.

Sea ice thickness observations from SMOS and CryoSat-2 have complementing uncertainties. SMOS has high uncertainties when measuring thick ice and CryoSat-2 has high uncertainties when measuring thin ice (Ricker et al., 2017b). This creates an opportunity for synergy between the instruments. The AWI CS2SMOS dataset takes advantage of this synergy. By combining
110 the datasets through a weighted averaging scheme, root mean squared errors are reduced from 76 cm with CryoSat-2 alone to 66 cm and the squared correlation coefficient is increased from 0.47 with CryoSat-2 to 0.61 when compared against NASA Operation Ice Bridge data (Ricker et al., 2017b). The AWI CS2SMOS dataset is available at a weekly time resolution and on a 25 km EASE-Grid 2.0 and was used with the method demonstrated here due to the high spatial coverage.

The NASA Operation IceBridge (OIB) mission is an airborne campaign comprising a series of flights covering the years
115 2009-2016, bridging the gap between the NASA Ice, Cloud and land Elevation Satellite (ICESat) and NASA ICESat-2 laser altimeter satellite missions (Kurtz et al., 2013). Among the instruments aboard each OIB flight, of primary importance to this study are the Airborne Topographic Mapper (ATM) instrument (Krabill et al., 1995) and snow radar (Panzer et al., 2013). The ATM is a laser altimeter whose return signal is used along with an aerial photography based sea ice lead (fracture) discrimination algorithm to retrieve sea ice freeboard height at 40 m spatial resolution. The snow radar return signal is used

120   to determine snow depth. Sea ice freeboard and snow depth are used in conjunction with a hydrostatic balance to determine sea ice thickness at the sea ice freeboard resolution of 40 m. We use OIB sea ice thickness from the IceBridge L4 Sea Ice Freeboard, Snow Depth, and Thickness, Version 1 and its QuickLooks counterpart as provided by the NSIDC (Kurtz et al., 2015). Figure 1 shows OIB flight paths used in this study.

2.4   Ice Mass Balance Buoys

125   In order to statistically characterize the sea ice thickness retrieval method described herein, ice mass balance buoy data served as the reference. The ice mass balance buoys were deployed and maintained by the United States Army Corps of Engineers Cold Regions Research and Engineering Laboratory (CRREL) (Perovich et al., 2021). Undeformed ice floes are chosen for buoy sites to ensure the buoy is representative of the surrounding ice (Polashenski et al., 2011).

    Data fields used from the buoys were sea ice thickness and geolocation in latitude and longitude. Ice thickness is observed
130   using two acoustic rangefinder sounders, one positioned above and one positioned below the ice. Each sounder has an accuracy of 0.005 m (Richter-Menge et al., 2006). An Argos antenna mounted on the buoy transmits the geolocation and other observations at minimum twice per day (Richter-Menge et al., 2006). For this study, all data fields were resampled to 1 d resolution by calculating daily mean values. All buoys from the years 2003 to 2016 showing an entire season of sea ice thickness growth were used for comparison with the exception of buoys installed in landfast ice and those that show obvious ice deformation
135   effects. Table 1 provides details pertaining to the buoys used. Buoy 2013F spanned two winter seasons and as such has been divided into two buoy numbers, 2013F and 2013Fb, with 2013Fb covering the second winter season during which the buoy was deployed. As such, a deployment date is not listed for 2013Fb. Drift tracks from 1 November to 1 April for the buoys are shown in Fig. 1. The buoys are concentrated in the Central Arctic and Beaufort Sea.

Table 1. A listing of United States Army Corps of Engineers Cold Regions Research and Engineering Laboratory (CRREL) Ice Mass Balance buoys used in this work. All buoys from 2003 to 2016 containing a full season of sea ice thickness growth are included, excluding those in landfast ice or showing obvious dynamic effects.

Buoy	Region	Ice Type	Deployment date
2003C	Beaufort Sea	Multi-year	2002/8/31
2005F	Central Arctic	Multi-year	2005/9/3
2006C	Beaufort Sea	Multi-year	2006/9/4
2012G	Central Arctic	First year	2012/10/1
2012H	Beaufort Sea	First year	2012/9/10
2012L	Beaufort Sea	Multi-year	2012/8/27
2013F	Beaufort Sea	Multi-year	2013/8/25
2013G	Beaufort Sea	Multi-year	2013/9/4
2013Fb	Beaufort Sea	Multi-year	-
2015F	Central Arctic	Multi-year	2015/8/13
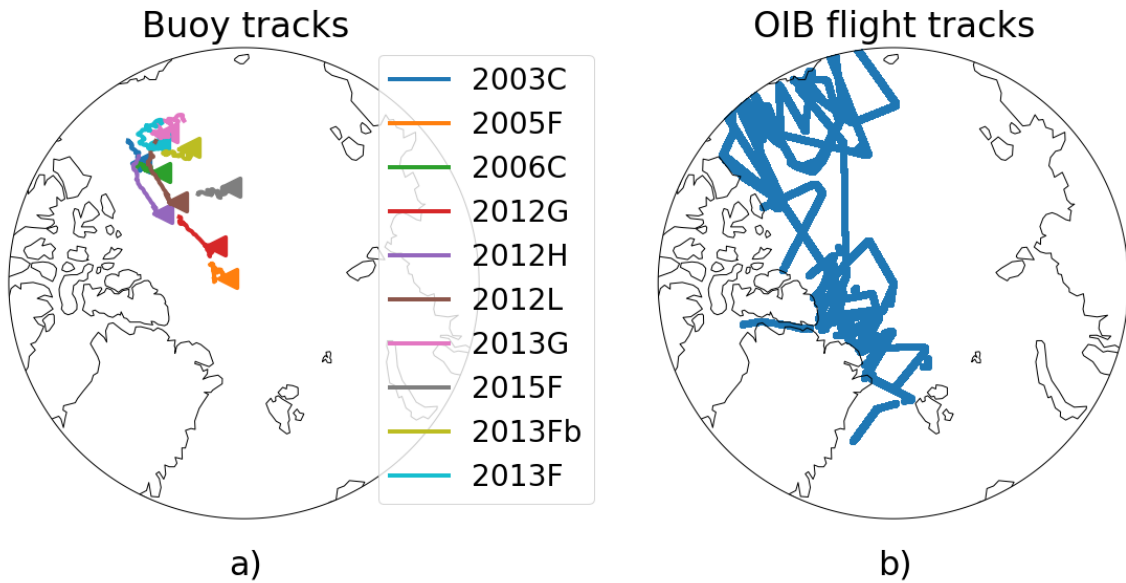
Figure 1. Tracks traveled by a) ice mass balance buoys and b) Operation IceBridge flights used in this study. Initial buoy location is signified with a left facing triangle and all buoy tracks from 1 November to 1 April.

Efforts to compare satellite based records of sea ice thickness with ground truth are hampered by the scale of the question. Ground truth measurements of sea ice are necessarily taken from a single point while satellites observe sea ice thickness on the scale of kilometers. The variability of sea ice across those kilometers leads to uncertainty in the comparison. It has been shown, however, that while variability in absolute ice thickness may be significant on the scale of a satellite observation, sea ice growth and melt are relatively uniform on the satellite length scale (Polashenski et al., 2011). Therefore, while absolute comparisons of sea ice thickness between a ground truth and satellite observation may be tenuous, comparisons of growth over a winter season between single point ground truth and satellite based observations are more robust.

2.5 Sea ice models

The Pan-Arctic Ice–Ocean Modeling and Assimilation System (PIOMAS) is a numerical model reanalysis product that couples the Parallel Ocean Program (POP) model developed at Los Alamos National Laboratory with a thickness and enthalpy distribution (TED) model (Zhang and Rothrock, 2003). The TED model includes a viscous–plastic sea ice rheology (Hibler, 1979) and a sea ice thickness distribution scheme that accounts for redistribution due to ridging (Thorndike et al., 1975). The model utilizes a generalized orthogonal curvilinear coordinate (GOCC) grid. The northern grid pole is shifted to be over Greenland where there is no ocean or sea ice, avoiding the need to deal with converging meridians and grid cell areas that approach zero. This shift also allows the highest grid resolutions to occur in the Canadian Archipelago, Baffin Bay and the Greenland Sea where the geography is intricate. The model is driven by daily surface forcing and sea surface temperatures (SSTs) provided by

NCEP/NCAR and NSIDC sea ice concentration in order to produce daily sea ice thickness distributions from 1978 to present (Schweiger et al., 2011). Here we use the daily effective sea ice thickness output which converts sea ice thickness distribution into a single effective thickness value for each grid cell.

Additionally, the data output from the sea ice model described in Kang et al. (2021), henceforth K21, was used to provide additional context. As briefly described in Sect. 1, K21 nudged a one-dimensional sea ice thermodynamic model with satellite retrieved snow–ice interface temperatures. The model itself is based on Maykut and Untersteiner (1971) and is a multi-layer numerical approximation for the snow and sea ice system. While the model is driven by European Centre for Medium-Range Weather Forecasts (ECMWF) ERA-Interim reanalysis data, temperatures at the snow–ice interface are nudged using the same snow–ice interface temperature retrieval used here (Lee and Sohn, 2015) in a non-physical correction term. This method was extrapolated to basin-wide results through the use of lagrangian tracking of individual sea ice parcels. The SLICE model is similar but greatly simplified and driven directly by the snow–ice interface temperature retrieval.

3 Methodology

Sea ice grows thicker through two primary physical mechanisms: thermodynamic phase change and dynamic changes due to the relative motion of the ice pack. The governing equation for a Eulerian sea ice thickness field can be written as

$$\frac{\partial H}{\partial t} = f(t, H, \mathbf{x}) - \nabla \cdot (\mathbf{u} H), \tag{1}$$

where H is plane slab sea ice thickness, t is time, f is a function of time, thickness and position vector $\mathbf{x}$ describing thermodynamic sea ice thickness increase, and $\mathbf{u}$ is the ice motion vector. This equation is analogous to Eq. (3) in (Thorndike et al., 1975), but does not include the redistribution term because here we use a plane slab thickness H rather than a thickness distribution. The second term on the right hand side of Eq. (1) captures dynamic thickness changes, including both advection and deformation of sea ice. Through the following methodology called Stefan's Law Integrated Conducted Energy (SLICE), we retrieve the first term on the right hand side of Eq. (1) and use a parcel tracking approach to approximate sea ice advection and model basin-wide thickness.

3.1 Snow–Ice Interface Temperature

Outgoing longwave radiation on the low frequency end of the microwave spectrum is not significantly absorbed by snow on the Earth's surface (Mathew et al., 2009). Previous efforts to take advantage of this fact to measure the temperature of sea ice have relied on infrared (IR) measurements or models to augment the results (Comiso, 1983; Hall et al., 2004; Hewison and English, 1999). This process leads to errors and IR data is only available in clear sky conditions. In Lee and Sohn (2015), only microwave brightness temperatures are used. The method uses the horizontally and vertically polarized 6.9 GHz channel brightness temperatures from the passive microwave AMSR-E or AMSR2 instruments along with a combined Fresnel relationship (Sohn and Lee, 2013) to determine the local microwave emissivity of sea ice. This emissivity along with the observed brightness temperatures yields the snow–ice interface temperature. In Lee et al. (2018), the method is adapted for use with the

SSM/I 19.35 GHz channel to allow for retrieval of snow–ice interface temperature beginning in 1987. We have adapted the procedure from Lee and Sohn (2015) for use in the retrieval method described below.

3.1.1 Atmospheric Transmittance

In order to accurately retrieve snow–ice interface temperature using passive microwave brightness temperatures, the effect of the atmosphere on these satellite observed brightness temperatures must be understood and accounted for. Atmospheric transmittance at 6.9 GHz was estimated using the Radiative Transfer for TOVS v12 (RTTOV v12; Saunders et al., 2018) radiative transfer model driven by ECMWF ERA5 reanalysis data (Hersbach et al., 2020, 2018).

The RTTOV model is capable of simulating brightness temperatures and other radiative characteristics of the Earth system as observed by roughly 90 space-borne sensors, including AMSR-E and AMSR2. For this study, the RTTOV direct radiative transfer model Python wrapper was used to simulate atmospheric transmittance for the AMSR-E and AMSR2 6.9 GHz channels, of which both vertical and horizontal polarizations yield the same results. The AMSRE and AMSR-2 satellite zenith viewing angle of $55°$ was accounted for along with a sea ice surface type. Temperature and humidity profiles at 37 pressure levels along with skin temperature, surface pressure, 2 m temperature, 2 m humidity and 10 m winds were provided by ERA5 reanalysis data at monthly temporal resolution and $1°$ spatial resolution from 2003 through 2020. The result is a dataset of monthly, $1°$ atmospheric transmittance for the 6.9 GHz AMSR-E and AMSR2 channels from 2003 to 2020 at monthly temporal and $1°$ spatial resolutions. These transmittance values were used in the calculation of snow–ice interface temperature.

3.1.2 Combined Fresnel Equation

Assuming absorption by snow is negligible, the snow–ice interface temperature can be related to satellite observed brightness temperature from a channel with a weighting function peak at the snow ice interface through the following two relationships:

$$T_{B,H}(\nu) = t_{atm}(\nu)\epsilon_H(\nu)T_{si} \tag{2}$$

$$T_{B,V}(\nu) = t_{atm}(\nu)\epsilon_V(\nu)T_{si}, \tag{3}$$

where $T_{B,H}(\nu)$ and $T_{B,V}(\nu)$ are satellite observed horizontally and vertically polarized spectral brightness temperatures, respectively, $t_{atm}(\nu)$ is spectral atmospheric transmittance, $\epsilon_H(\nu)$ and $\epsilon_V(\nu)$ are local snow–ice interface spectral emissivity for horizontal polarized and vertical polarized emission, respectively, and T_{si} is snow–ice interface temperature.

Eqs. (2) and (3) form a system of two equations with three unknowns—$\epsilon_H(\nu)$, $\epsilon_V(\nu)$ and T_{si}. Assuming reflectivity and emissivity sum to unity in both polarizations, a combined Fresnel relationship closes this system and allows solving for T_{si}:

$$r_V(\nu) = \left(r_H(\nu)^2 \frac{1 + r_H(\nu)^{-1/2}\cos 2\theta}{1 + r_H(\nu)^{1/2}\cos 2\theta} \right)^2, \tag{4}$$

where θ is satellite viewing angle, and $r_H(\nu)$, $r_V(\nu)$ are horizontal and vertical polarized spectral reflectance, respectively. Additional detail can be found in Lee and Sohn (2015).

Liquid water at the emitting layer in the form of open ocean or melt ponds interferes with the snow–ice interface temperature algorithm (Lee and Sohn, 2015). As such, and in line with Lee and Sohn (2015), the snow–ice interface is only calculated here
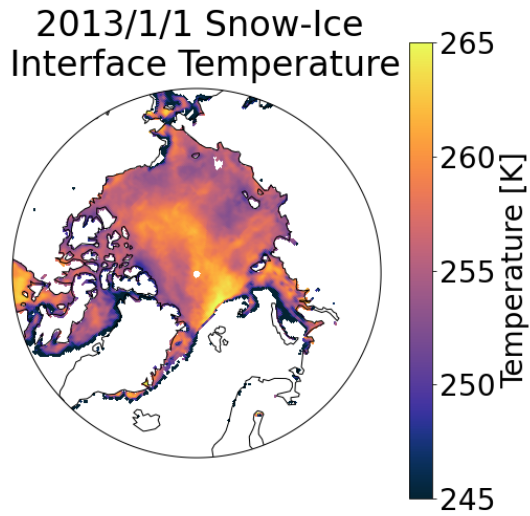
Figure 2. Snow–ice interface temperatures on 1 January 2013 derived from AMSR2 radiances.

in grid cells with greater than 95% sea ice concentration. A method for calculating snow–ice interface temperature for grid cells with under 95% sea ice concentration is described in the appendix of Lee and Sohn (2015) but is not implemented here pending further investigation.

220 ## 3.2 Thermodynamic sea ice thickness growth

A simple model of one-dimensional thermodynamic sea ice thickness growth is a balance of heat fluxes where phase change is occurring, i.e., at the interface between the solid sea ice and liquid sea. These heat fluxes are latent heat released during the phase change of liquid sea water to solid sea ice, F_l, basal heat flux from the liquid sea to the solid ice, F_w, and heat conducted through the ice and away from the phase change interface, F_c. These three fluxes are balanced at the phase change interface as 225 follows:

$$F_l + F_w = F_c. \tag{5}$$

When the snow–ice interface temperature drops below the temperature at the bottom of the ice, heat provided by basal flux and the latent heat of freezing is pulled to the snow–ice interface. In the method described here, a satellite observation of snow–ice interface temperature (Lee and Sohn, 2015) drives this energy balance in order to determine sea ice thickness growth.

3.2.1 Stefan's Law

By balancing the conductive heat equation with a latent heat of freezing and basal heat flux term, Stefan's Law relates the rate of thermodynamic sea ice thickness increase to the temperature difference between the snow–ice interface and bottom of the ice layer, the later of which is at or very near to the freezing temperature of sea ice (Stefan, 1891; Lepparanta, 1993).

Just as fluid flows across a pressure difference and electricity flows across a voltage difference, all heat transfer occurs across a temperature difference. Conduction is the transfer of heat across a solid medium and is always accompanied by a temperature difference across that medium. The equation governing one-dimensional, steady state conduction through sea ice is

$$F_c = \frac{\kappa_{eff}}{H}\left(T_f - T_{si}\right), \tag{6}$$

where κ_{eff} is the thermal conductivity of sea ice, H is sea ice thickness, T_f is the freezing point of sea water and T_{si} is the snow–ice interface temperature.

A change in the phase of a material must either release or accept energy as the molecular bonds and motion within the material change. In the case of a phase change from liquid to solid, energy is released as the molecular motion is reduced with the introduction of molecular bonds. The equation describing the one-dimensional, latent heat release as sea water changes phase from liquid to solid is:

$$F_l = \rho_i L \frac{dH}{dt}, \tag{7}$$

where ρ_i is the density of the solid phase of the material, L is the latent heat of fusion and $\frac{\partial H}{\partial t}$ is the change in sea ice thickness per unit time.

In Stefan's Law, Eqs. (6) and (7) are substituted into Eq. (5) to form

$$\rho_i L \frac{\partial H}{\partial t} = \frac{\kappa_{eff}}{H}\left(T_f - T_{si}\right) - F_w. \tag{8}$$

Isolating for sea ice thermodynamic growth rate, we have

$$\frac{\partial H}{\partial t} = \frac{\kappa_{eff}}{\rho_i L H}\left(T_f - T_{si}\right) - \frac{F_w}{\rho_i L}. \tag{9}$$

Equation (9) defines the thermodynamic growth function, f, found in Eq. (1) and is equivalent to Eq. (1) when dynamic growth is neglected. There are three assumptions inherent to this relationship (Lepparanta, 1993). First, heat conduction in the horizontal direction is assumed to be negligible. Second, it is assumed that there is no thermal inertia present in the ice. This means that the local derivative of temperature with respect to sea ice depth is constant throughout the sea ice layer—i.e., the temperature profile is linear—and the system is in equilibrium. The spatial derivative of temperature found in a typical heat equation reduces to the temperature difference between the snow–ice interface temperature and the freezing point of water due to these first two assumptions. Third, it is assumed that there is no internal heat source, such as the absorption of short wave radiation. The second and third assumptions are only valid during polar winter and times of the year when solar incidence angles are very shallow.

Eqs. (8) and (9) are differential equations with the following solution:

$$H = \sqrt{H_0^2 + \delta t \frac{2\kappa_{eff}}{\rho_i L}(T_f - T_{si})} - \delta t \frac{F_w}{\rho_i L}, \tag{10}$$

where H_0 is the initial sea ice thickness. The time interval δt chosen for the results shown herein is one day based on the daily availability of snow–ice interface temperature and both snow–ice interface temperature and basal flux are assumed to be constant during each day.

At each time step, SLICE determines sea ice thickness by solving Eq. (10) for H given an H_0 using the snow–ice interface temperature calculated at the nearest AMSR-E or AMSR2 grid cell. The change in sea ice thickness at each time step is dependent on initial sea ice thickness. This necessitates SLICE be applied in a Lagrangian sense as the sea ice thickness must be tracked and stored in order to accurately calculate the change at the next time step. In Eq. (9), thicker sea ice grows slower than thinner sea ice and thinner sea ice grows faster than thicker ice with a given snow–ice interface temperature. This means that in the presence of only thermodynamic effects, sea ice that is too thick or too thin will correct towards the unbiased SLICE thickness profile. This relationship replicates the phenomenon described in Bitz and Roe (2004), whereby thick ice grows slower than thin ice and vice versa.

3.2.2 Basal flux

Observation of basal flux from liquid sea water to solid sea ice is inherently difficult. Typically, basal flux is calculated as a residual of other more readily observed quantities in the heat budget of a one-dimensional sea ice profile, typically from a drifting station or buoy. Using this methodology, McPhee and Untersteiner (1982) observed March through May basal fluxes of less than 2 W m^{-2} using data from the FRAM I drift station in the Arctic Ocean, Perovich and Elder (2002) report oceanic heat flux values of just a few W m^{-2} from November to May during the Surface HEat Budget of the Arctic Ocean (SHEBA) field experiment and Lei et al. (2014) examined Chinese National Arctic Research Expedition (CHINARE) buoy data to discover relatively high basal ocean heat fluxes of greater than 10 W m^{-2} through December that gradually decreased to near 0 by mid-February.

Maykut and Untersteiner (1971) completed a sensitivity analysis using their thermodynamic sea ice model, investigating the equilibrium mean annual sea ice thickness corresponding to basal flux values ranging from 0 to 8 W m^{-2}. Realistic mean annual sea ice thickness resulted when basal flux was set between 1.3 W m^{-2} and 2.6 W m^{-2}. They chose a constant basal flux value of 2 W m^{-2} for their model based on this analysis and available observational data. The coupled ocean–sea ice model PIOMAS supplies oceanic heat fluxes to the sea ice model component as modeled by the ocean model component. Zhang and Rothrock (2003) show these modeled ocean heat fluxes in most of the Arctic basin to be near 2 W m^{-2}. K21 also employed a constant basal heat flux of 2 W m^{-2}.

In keeping with these studies, we apply a constant basal oceanic heat flux $F_w = 2$ W m^{-2}. The effect of basal oceanic heat flux on thermodynamic sea ice growth is independent of thickness and can be easily quantified as the last term of Eq. (10). For a given snow—ice interface temperature, the reduction of sea ice thickness growth by inclusion of a basal flux is linearly related to the basal flux value by a factor of $1/\rho_i L$. With a density of 917 kg m^{-2} and a latent heat of fusion of 3.32 x 10^5 J

kg^{-1}, each 1 W m^{-2} of basal flux from the liquid sea water to solid sea ice decreases sea ice thickness growth by 2.84×10^{-4} m d^{-1}. Removal of the 2 W m^{-2} basal oceanic heat flux would increase sea ice growth by 5.67×10^{-4} m d^{-1} and an increase from 2 W m^{-2} to 10 W m^{-2} would decrease thermodynamic sea ice thickness growth by 2.27×10^{-3} m d^{-1}. This corresponds to a 0.0857 m increase and a 0.343 m decrease, respectively, when summed from 1 November to 1 April.

3.2.3 Multi-phase properties of sea ice

Sea ice is best described not as a homogeneous solid media but rather as a heterogeneous, multi-phase material including solid ice and pockets of liquid brine whose size and salinity change with varying ice temperatures. In turn, these brine pocket changes significantly affect the bulk thermodynamic properties of the ice layer (Feltham et al., 2006). Equation (10) includes effective thermal conductivity, κ_{eff}, a property that is subject to this effect. As such, we adopt the parameterization of effective conductivity described in Feltham et al. (2006).

We begin by defining a constant ocean salinity, S, of 33 ppt. Next, we will assume that the ice is in thermal equilibrium relative to phase change between liquid brine and solid ice and calculate freezing point temperature (in °C), T_f, as a function of salinity (in ppt) per Notz (2005):

$$T_f(S) = -0.0592S - 9.37 \times 10^{-6}S^2 - 5.33 \times 10^{-7}S^3. \tag{11}$$

The latent heat of fusion for liquid to solid phase change is defined as the difference between the enthalpies of the two states. In this case, we will use a latent heat of fusion (in J kg^{-1}), L as calculated as a function of temperature (in °C) by Notz (2005):

$$L(T_f) = 333700 + 762.7T_f - 7.929T_f^2. \tag{12}$$

We then use Eq. (15) from Feltham et al. (2006) to define effective thermal conductivity (in W m^{-1} K^{-1}) as function of sea ice temperature, T_i and sea ice salinity, S_i:

$$\kappa_{eff} = \kappa_{bi} - (\kappa_{bi} - \kappa_b)\frac{(T_f(0) - T_f(S_i))}{(T_f(0) - T_i)}, \tag{13}$$

where κ_{bi} is the thermal conductivity of bubbly ice and κ_b is the thermal conductivity of liquid brine and are defined per Schwerdtfecer (1963), Batrak et al. (2018) and Bailey et al. (2010) (all in W m^{-1} K^{-1}):

$$\kappa_{bi} = \kappa_i(2\kappa_i + \kappa_a - 2V_a(\kappa_i - \kappa_a))/(2\kappa_i + \kappa_a + 2V_a(\kappa_i - \kappa_a)) \tag{14}$$

$$\kappa_b = 1.162(0.45 - 1.08 \times 10^{-2}T + 5.04 \times 10^{-5}T^2) \tag{15}$$

$$\kappa_i = 1.162(1.905 - 8.66 \times 10^{-3}T + 2.97 \times 10^{-5}T^2) \tag{16}$$

$$\kappa_a = 0.03 \tag{17}$$

$$V_a = 0.025, \tag{18}$$

where κ_i is the thermal conductivity of pure ice, κ_a is the thermal conductivity of air and V_a is the fractional volume of air in the sea ice. We will use effective conductivity calculated with surface conditions for SLICE which is similar to the approach

adopted by Cox and Weeks (1988) who also used conductivity calculated from the surface to determine conductive flux through the ice layer.

325   A first-year sea ice (FYI) density of 917 kg m^{-3} and multi-year sea ice (MYI) density of 882 kg m^{-3} was reported by Alexandrov et al. (2010) and these values have seen use in the sea ice thickness calculations from CryoSat-2 data (Laxon et al., 2013; Tilling et al., 2018; Hendricks and Ricker, 2020; Kwok and Cunningham, 2015). A sea ice density of 915 kg m^{-3} is also in use with altimeter data (Kurtz et al., 2014b; Petty et al., 2020) and a sea ice density of 925 kg m^{-3} has been used with IceSat data (Kwok and Rothrock, 2009). Choice of sea ice density is a significant source of uncertainty in altimeter-based estimates

330   of sea ice thickness. Kurtz et al. (2014b) report that the range of densities from 882 kg m^{-3} to 925 kg m^{-3} yields a 1.1 m range in sea ice thickness estimates from a 60 cm snow—ice freeboard with 35 cm of snow. The SLICE system of equations uses a FYI sea ice density of 917 kg m^{-3}. For a given snow—ice interface temperature, basal flux and sea ice thickness, a change to 915 kg m^{-3} would increase sea ice thickness growth rate by at most only 0.2% and a change to 925 kg m^{-3} would decrease sea ice thickness growth by at most only 0.8%.

335 ### 3.3   Parcel tracking of advection

The divergence term on the right hand side of Eq. (1) represents sea ice dynamics and includes the effects of both advection and deformation on local sea ice thickness. Advection moves sea ice parcels horizontally and deformation redistributes sea ice volume vertically through ridging or leading.

    The advection effects contained within the divergence term can be approximated using a parcel tracking approach, allowing

340   for the modelling of basin-wide results. This parcel tracking methodology is initialized with the CS2SMOS data from the first week of November and each 25 km x 25 km grid cell is divided into 5 km x 5 km parcels, which are advected daily throughout the winter using the Polar Pathfinder motion vectors interpolated to their position. This parcel tracking methodology is similar to the Sea Ice Tracking Utility (SITU, http://icemotion.labs.nsidc.org/SITU/) described by DeRepentigny et al. (2016). Each parcel adds sea ice thickness thermodynamically using the SLICE thermodynamic model. At any given time step, the parcels

345   can be gridded to the EASE-Grid 2.0 by taking the mean thickness of parcels within each grid cell. This approach leaves out deformation effects. While taking the sum of all parcel volume within each grid cell and dividing by grid cell area would be a more physically sound methodology for this regridding, the results from such a method proved unrealistic. Figure A2 found in the Appendix shows a comparison between the chosen method using grid cell mean and the method using grid cell sum. New parcels are initiated at any grid cell not containing a sea ice parcel but showing 95% or greater sea ice concentration. New ice

350   parcels are initialized at 0.05 m. Any parcel that is located in a region with less than 95% sea ice concentration at any time step is removed. The result is a daily gridded Arctic basin-wide sea ice thickness dataset representing thermodynamic sea ice growth in the 95% sea ice concentration ice pack.

4 Results

The SLICE sea ice thickness retrieval methodology can be applied on a single one-dimensional profile basis or across a large area. Here we present results comparing one-dimensional profiles to ice mass balance buoy thicknesses and Arctic basin-wide results compared to OIB and AWI CS2SMOS data.

4.1 One-dimensional Profiles

The SLICE retrieval method results were compared to sea ice thickness from ice mass balance buoys. The retrieval method was initialized with the buoy observed sea ice thickness on 1 November and integrated through 1 April. The retrieval method is dependent only on the satellite based snow–ice interface temperature. The snow–ice interface temperature used on a given day is taken from the nearest AMSR-E or AMSR2 grid cell to the buoy location. The resultant sea ice thickness time series are plotted with buoy sea ice thickness in Fig. 3. It is clear from Fig. 3 that the SLICE profiles agree well with the buoy sea ice thickness when initialized with an accurate initial ice thickness. The correlation coefficients ranges from 0.37 to 0.999 with a mean of 0.88 and standard deviation of 0.21 across all buoys. The bias, calculated by taking the mean over the entire profile length of the retrieval method result minus the buoy thickness, ranges from -0.01 m to 0.19 m with a mean of 0.08 m and standard deviation of 0.07 m across the buoys.

4.2 Arctic Basin-wide Comparisons

Next, the SLICE retrieval method was utilized to model sea ice thickness on a Arctic basin-wide scale. Using the AWI CS2SMOS data for the first week of November as the initial state, the retrieval method was applied daily to the entire Arctic basin from 1 November to 1 April for the growth seasons beginning in 2012 through 2019. November first was chosen to ensure most ice was below the freezing point and there were limited melt ponds to interfere with the snow ice interface temperature observation. At each time step, the parcel tracking methodology described in Sect. 3.3 is applied. The 1 April results are regridded to the 25 km EASE-Grid 2.0 using the procedure also described in Sect. 3.3. Monthly basin-wide sea ice thickness plots for the sea ice growth season beginning in fall 2012 using AWI CS2SMOS as the initial state are shown in Fig. 4. The sea ice thickness data from SLICE is available daily but only the first of every month is plotted. The sea ice thickness is increasing and advection is relocating the volume horizontally throughout the Arctic basin.

In order to compare SLICE with PIOMAS and K21 data, all three datasets were compared with OIB sea ice thickness observations. OIB data from the month of March for the years 2013 through 2018 (including NSIDC OIB quick looks data) was first binned by 25 km EASE 2.0 grid cell and averaged across each bin to create an OIB dataset collocated with SLICE. Both PIOMAS and the K21 data were also interpolated to the 25 km EASE 2.0 grid. A comparison between SLICE, PIOMAS and K21 was created and shown in Fig. 5. Linear correlation and bias statistics were calculated from this data. All three datasets show very similar linear correlations of 0.67, 0.67 and 0.68 for SLICE, PIOMAS and K21, respectively. The best mean bias is PIOMAS at 0.10 m, followed closely by SLICE at -0.12 and K21 at -0.24 m. The standard deviation of the bias is 0.68 for both PIOMAS and SLICE and nearly the same for K21 at 0.69.
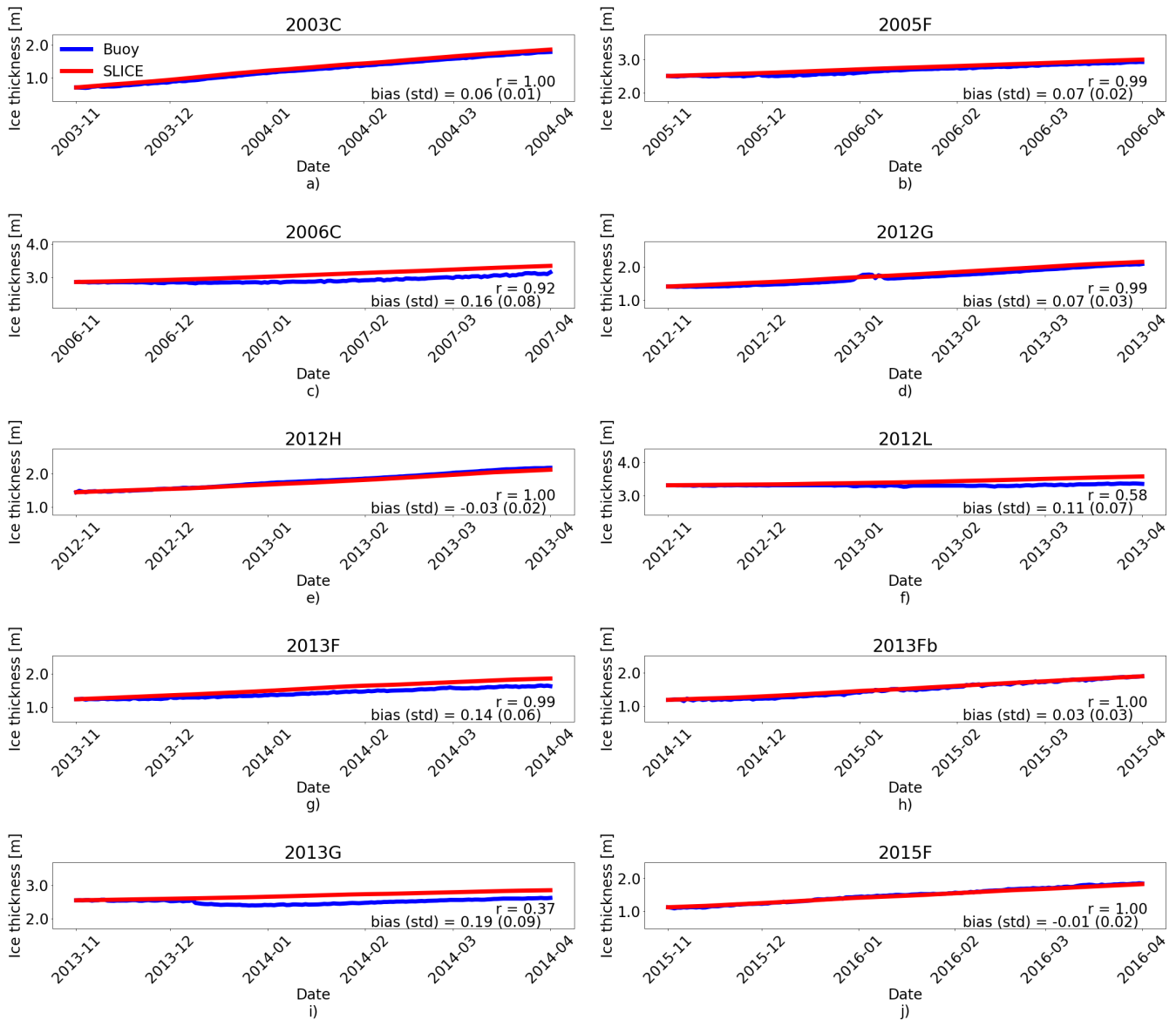
Figure 3. Ice thickness observations from ice mass balance buoys and SLICE for buoys (a) 2003C, (b) 2005F, (c) 2006C, (d) 2012G, (e) 2012H, (f) 2012L, (g) 2013F, (h) 2013Fb, (i) 2013G and (j) 2015F. Linear correlation (r) and bias values are listed. Across all buoys, the r values have a mean of 0.88 and the biases have a mean of 0.08 m.

SLICE was also compared to PIOMAS using AWI CS2SMOS as the reference dataset. Figure 6 shows the differences in sea ice thickness between SLICE and AWI CS2SMOS and the differences between PIOMAS and AWI CS2SMOS on 1 April for the years 2013 through 2020. Figure A1 in the Appendix shows plots of sea ice thickness used in this comparison from all three datasets. The differences are almost all between -1.5 m and 1.5 m and in most cases are near zero. The difference plots
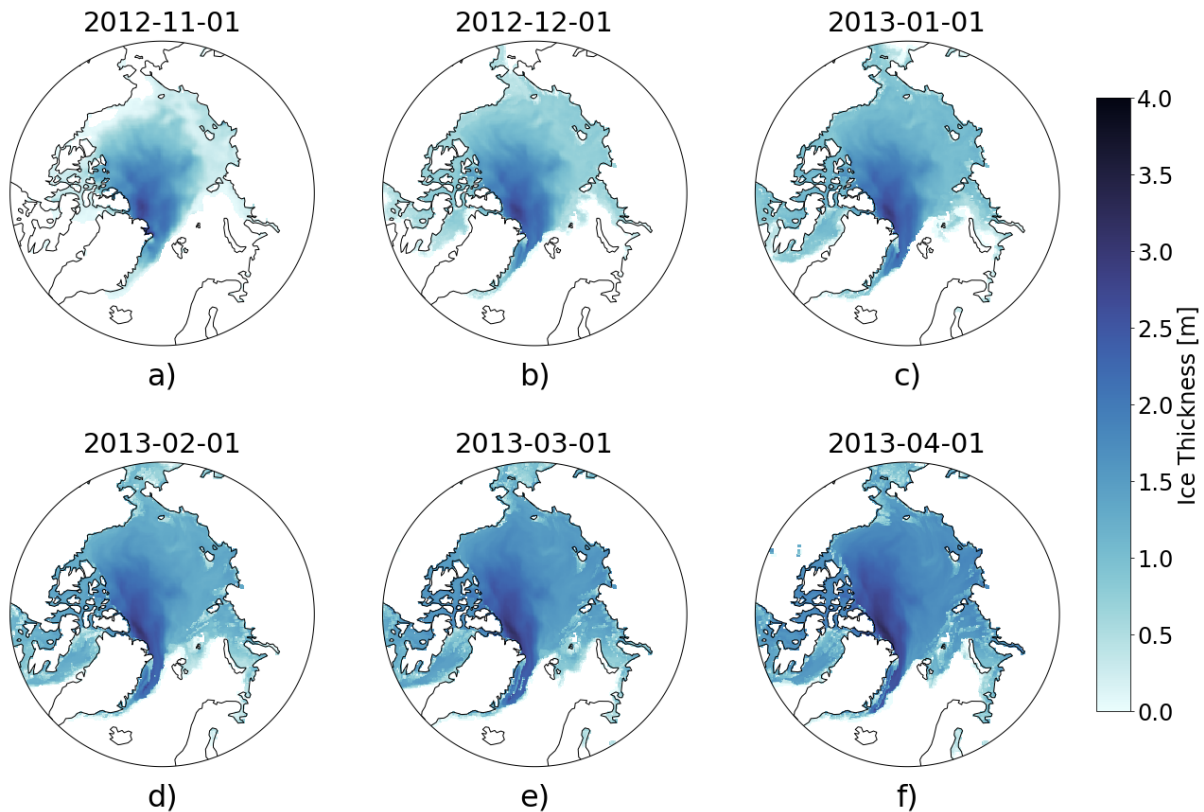
Figure 4. Sea ice thickness on a) 2 November 2012, b) 1 December 2012, c) 1 January 2013, d) 1 February 2012, d) 1 March 2013, e) 1 April 2013, f) 30 April 2013 created using SLICE with the 1 November 2012 AWI CS2SMOS as an initial state. The changes from month to month represent thermodynamic growth and advection.

for SLICE and PIOMAS show similar patterns, though PIOMAS overestimates thickness in more areas than SLICE, which
390   underestimates sea ice thickness in the central Arctic in almost all cases. The differences between SLICE and CS2SMOS
are likely to be due to a lack of deformation effects. Figure 7 shows a scatter plot of AWI CS2SMOS sea ice thickness to
sea ice thickness from SLICE and from PIOMAS. Both AWI CS2SMOS and SLICE are on a 25 km EASE-Grid 2.0 but
in order to compare the AWI CS2SMOS data to PIOMAS, it is interpolated to each PIOMAS grid point. Linear correlation
and bias statistics were calculated from this data. SLICE and PIOMAS have equal linear correlations with AWI CS2SMOS
395   at 0.77. SLICE shows an improved mean bias at 0.03 m compared to PIOMAS at 0.10 m. SLICE standard deviation of the
difference is also improved at 0.62 compared to 0.67 m for PIOMAS. Figure 8 shows total daily Arctic sea ice volume from
SLICE, PIOMAS and AWI CS2SMOS during the winters from late 2012 to early 2020. The AWI CS2SMOS is taken from the
the weekly data centered on each day. Both SLICE and PIOMAS follow the AWI CS2SMOS volume profile well. PIOMAS
overestimates end of season volume in all years and underestimates initial volume in all cases except 2012-2013 and 2016-
400   2017 leading to an overestimation of sea ice volume growth in all years. SLICE begins each season at the same volume as AWI
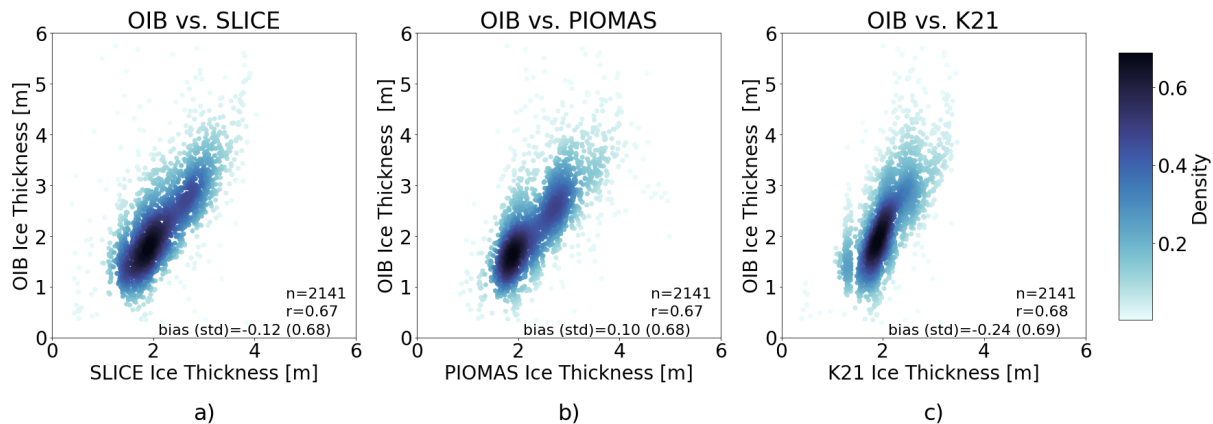
Figure 5. OIB thickness versus a) SLICE intilialized with CryoSat-2/SMOS, b) PIOMAS and c) Kang et al., 2021 data including number of data points, linear correlations and bias (standard deviation). SLICE has the highest linear correlation though all three are virtually equal.

CS2SMOS and ends all seasons closer than PIOMAS to the AWI CS2SMOS volume except 2014-2015 and 2016-2017. While there are not enough data points for a strong statistical comparison, SLICE is certainly a viable indicator of sea ice volume growth.

5 Discussion

405 SLICE uses a new retrieval of snow–ice interface temperature (Lee and Sohn, 2015) to drive a very simple one-dimensional model of sea ice thermodynamics in order to retrieve thermodynamic sea ice thickness growth. By applying SLICE to individual parcels whose location throughout the Arctic basin is determined using a sea ice motion product (Tschudi et al., 2020), SLICE is able to capture sea ice advection and produce basin-wide results. In doing so, SLICE functions similarly to much more intricate sea ice models such as PIOMAS (Zhang and Rothrock, 2003) and a sea ice model that is nudged with retrieved

410 snow–ice interface temperature (Kang et al., 2021). While SLICE is capable of capturing thermodynamic sea ice growth and advection, it is unable to detect deformation effects—i.e., thickness changes due ridging or leading.

Figure 3 shows a comparison between ice mass balance buoy sea ice thickness measurements and the retrieval method initialized with the buoy data for 10 buoys within the years 2003–2016. The mean correlation coefficient of 0.88 between the buoy measurements and the method is high. The bias values are also very encouraging with a mean of 0.08 m. Buoys 2012L

415 and 2013G have linear correlation values of 0.58 and 0.37, respectively, both significantly lower than the others. These buoys may have experienced delayed ice growth that begins later than 1 November or perhaps even melting. SLICE is unable to capture either phenomena, degrading the results from these buoys. The median linear correlation across all buoy results is 0.992 and the mean linear correlation from all buoys except 2012L and 2013G is 0.985. When sea ice is indeed increasing via thermodynamics, SLICE captures the growth well. Additionally, SLICE has a self-correcting quality by nature of Eq. (9)

420 whereby sea ice thicknesses that are biased in either direction approach the unbiased SLICE sea ice thickness over time. These
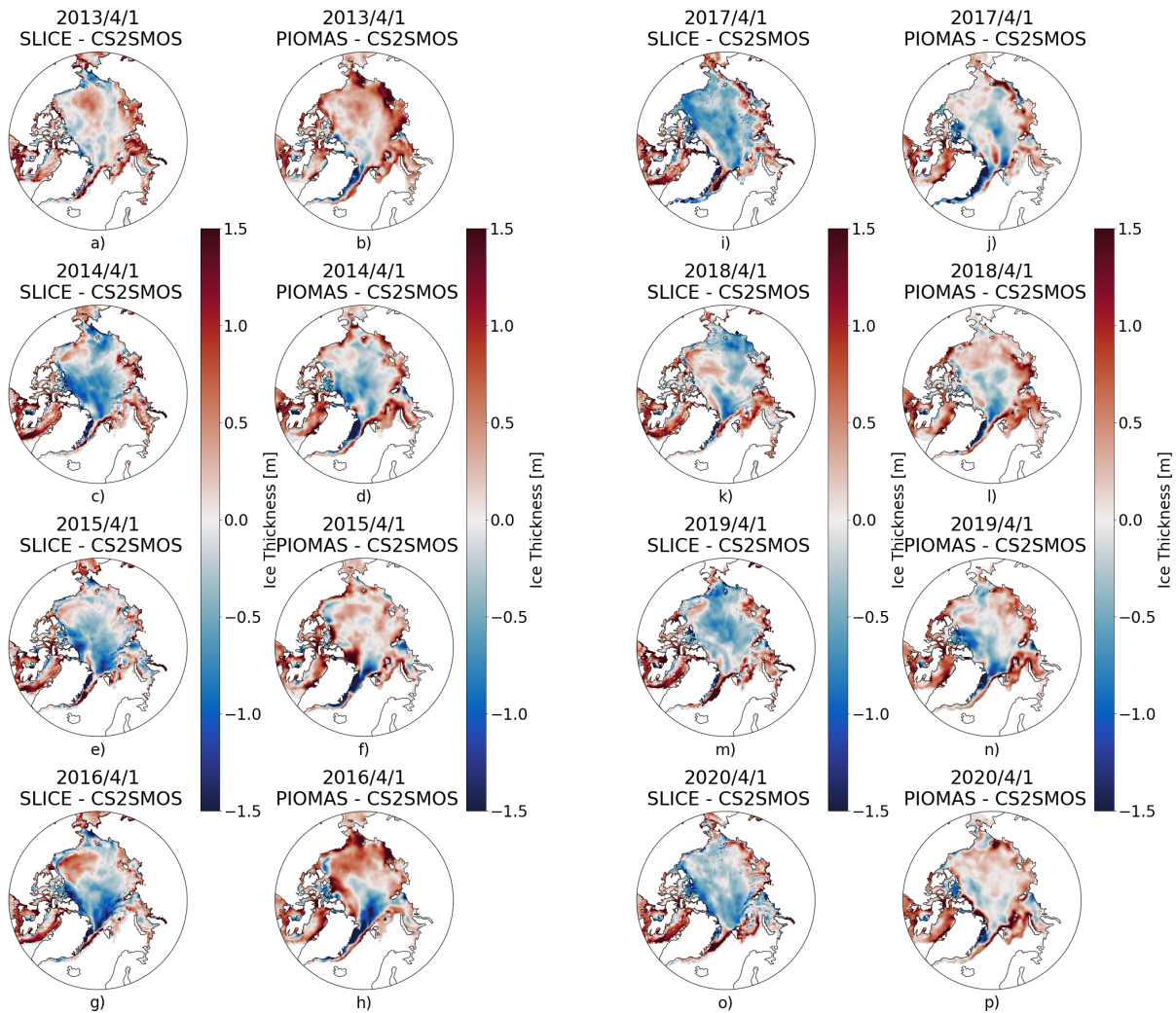
Figure 6. For the sea ice growth seasons ending in a–b) 2013, c–d) 2014, e–f) 2015, g–h) 2016, i–j) 2017, k–l) 2018, m–n) 2019 and o–p) 2020, a, c, e, g, i, k, m, o) SLICE sea ice thickness - AWI CS2SMOS sea ice thickness from 1 April and b, d, f, h, j, l, n, p) PIOMAS sea ice thickness - AWI CS2SMOS sea ice thickness from 1 April. The SLICE and PIOMAS differences show similarities in their overall pattern.

points suggest the retrieval method is viable as a basis for modelling sea ice thickness but is highly dependent on an initial condition, as it calculates thermodynamic sea ice thickness increase rather than absolute thickness.

There are a number of assumptions inherent to Stefan's Law (Lepparanta, 1993) that must be considered in relation to SLICE as introduced in Sect. 3.2. In order to characterize conduction through the ice layer with only the snow–ice interface temperature and an assumed freezing point temperature at the bottom of the ice layer, it must be assumed that heat conduction in the horizontal is negligible and that the local vertical derivative of temperature throughout the ice layer is constant. These assumptions are reasonable. The remaining two assumptions are more salient. The first is that there is no internal heat source.

425
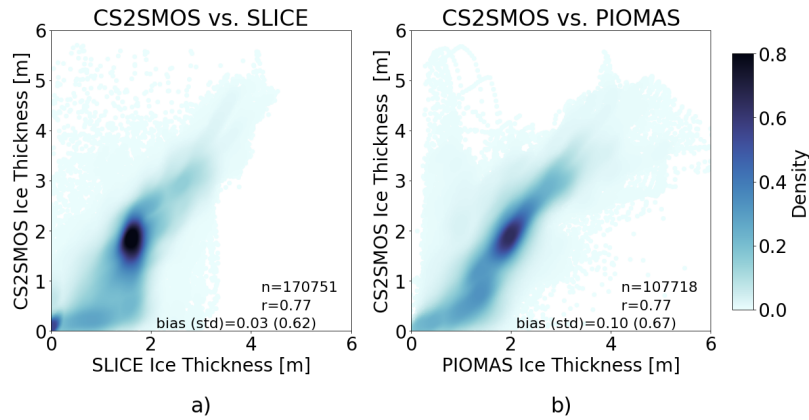
Figure 7. AWI CS2SMOS sea ice thickness versus a) SLICE sea ice thickness and b) PIOMAS sea ice thickness including number of data points, linear correlations and bias (standard deviation). SLICE has as lower bias at 0.03 m than PIOMAS at 0.10 m and linear correlation values are equal.
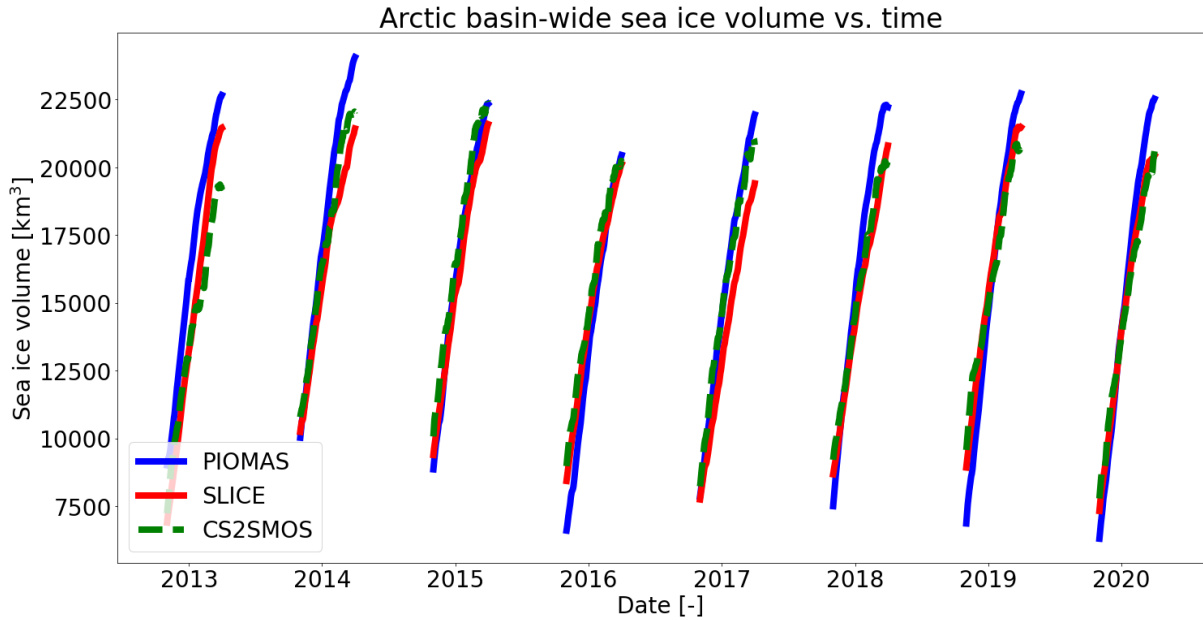
Figure 8. Wintertime sea ice volume versus time for SLICE, PIOMAS and AWI CS2SMOS.

This is untrue when there is significant short wave radiation absorbed within the sea ice. The final assumption is that heat exchange between the sea ice and the ocean is constant in space and time, which is likely to be invalid in some regions. Impacts of this assumption on the sea ice growth are investigated in Sect. 3.2.2.

Another source of uncertainty in SLICE ice thickness is the constraint that it is limited to areas with sea ice concentration greater than 95%. There is significant growth in areas where the sea ice concentration is low, such as the marginal ice zone (MIZ). This constraint would likely cause underestimated sea ice growth over those areas. In a supplement to the body of the paper, Lee and Sohn (2015) suggest a procedure for calculating snow–ice interface temperature in areas with less than 95% but that has not been implemented here, pending further investigation. Further validation of SLICE, particularly in regions other than the Beaufort Sea and Central Arctic, where all buoys and OIB flights used here were located, as well as investigation of the impacts of these assumptions and full characterization of uncertainties is warranted.

The Stefan's Law energy balance relationship and attendant assumptions amounts to a simplification the multi-layer thermodynamic model based on Maykut and Untersteiner (1971) that makes up the foundations of PIOMAS and K21. These assumptions remove the need for multiple layers. Additionally, whereas the thermodynamics in PIOMAS and K21 are driven by an atmospheric reanalysis product and nudged by snow–ice interface temperature in the case of K21, SLICE is driven by satellite observed snow–ice interface temperature. These factors allow for the instantaneous retrieval of thermodynamic thickness growth rate. Whereas PIOMAS models sea ice motion again using atmospheric reanalysis, SLICE uses a sea ice motion satellite product when used to model basin-wide sea ice thickness. This sea ice motion product and the snow–ice interface temperature product mean SLICE is heavily observationally constrained. The comparison between SLICE, PIOMAS and K21 show that these assumptions and simplifications do not degrade resultant sea ice thickness values when SLICE thermodynamic growth rate is used to model absolute thickness on a basin-wide scale, even without a deformation component.

Figure 8 is encouraging for the capability of SLICE to capture volumetric sea ice changes on a basin-wide scale. Per the model described by Eq. (1), sea ice volume is only added through thermodynamic processes—dynamic processes only serve to rearrange the volume already present. Though this statement does invoke the false assumption that dynamic processes do not change the density of the ice, it seems to be a factor in explaining the volumetric results. Though dynamic processes do not directly change sea ice volume, their changing of the thickness of ice at a given location does impact thermodynamic processes by virtue of f being a function of thickness, H, in Eq. (1). Inspection of Eq. (8) indeed shows that H impacts $\frac{\partial H}{\partial t}$. In regions where deformation increases sea ice thickness, SLICE will overestimate sea ice thickness increase and in regions where deformation decreases sea ice thickness, it will underestimate sea ice thickness increase. These phenomena, along with any phenomena inherent to either reference dataset, may explain volumetric differences between SLICE and the reference datasets.

6 Conclusions

New methods for observing snow–ice interface temperature (Lee and Sohn, 2015) have made possible a new strategy for observing thermodynamic sea ice thickness growth from space during the winter growth season: Stefan's Law Integrated Conducted Energy (SLICE). The new strategy involves coupling observed satellite retrieved snow–ice interface temperature with Stefan's Law (Stefan, 1891; Lepparanta, 1993). In the Stefan's Law relationship, latent heat of fusion is conducted from the bottom of the ice layer where new ice forms to the snow–ice interface and this rate of conduction and accretion is calculated using the snow–ice interface temperature and a parameterized freezing point temperature at the bottom of the ice layer. The

snow–ice interface temperature retrieval algorithm used to drive the sea ice thickness growth equation uses passive microwave brightness temperatures from the AMSR-E and AMSR2 instruments (Lee and Sohn, 2015). Gridded brightness temperature data from these instruments are available at daily temporal resolution in the polar regions (Cavalieri et al., 2014; Markus et al., 2018), meaning modelled daily sea ice thickness growth is available basin-wide. Lee et al. (2018) provides a method for retrieving snow–ice interface temperatures using passive microwave brightness temperatures from the SSM/I and SSMIS instruments, allowing for the application of SLICE to sea ice growth seasons beginning in 1987. SLICE requires an initial sea ice thickness value is required and does not capture melting.

When SLICE is initialized with an ice mass balance buoy thickness and compared against that buoy's ice thickness profiles during the ice growth season, the retrieval method compares well with the buoy observed sea ice thickness growth. Using ten buoys from 2003 to 2016, the mean linear correlation value is 0.88 and the mean bias is 0.08 m. SLICE can be used to model basin-wide sea ice thickness by applying the thermodynamic growth retrieval to individual sea ice parcels and advected the parcels across the basin using a sea ice motion product. This basin-wide methodology was applied to the winters between late 2012 and early 2020 using AWI CS2SMOS basin-wide sea ice thickness as the initial state. Results show that SLICE performs comparably to PIOMAS and K21, despite the assumptions and simplification that allow for the direct retrieval of instantaneous thermodynamic growth rate.

Current state of the art sea ice thickness observations from space, though capable of observing sea ice growth whether from thermodynamic or dynamic effects, are not capable of this spatial and temporal coverage. They also do not discriminate between dynamic and thermodynamic effects. For these reasons, a sea ice thickness dataset based on SLICE will be especially qualified for investigating thermodynamic and dynamic sea ice phenomena that are small scale in space and time. SLICE need not be initialized at the beginning of the growth season and applied for an entire growth season but can be initialized at any time during the growth season and applied to any interval of time, allowing for use with case studies or other small time and space scale events. Additionally, the high temporal resolution retrieval of thermodynamic effects will allow for creation of useful datasets of surface energy flux from latent heat of fusion.

Code and data availability. Data used in creation of all figures is available at https://doi.org/10.5281/zenodo.6554832. Code for creation of data and figures is available at https://doi.org/10.5281/zenodo.6561431 and https://github.com/janheuser/SLICE/releases/tag/1.0.0. The following auxilliary datasets were used and are available at these locations: AMSR-E and AMSR2 brightness temperatures, https://doi.org/10.5067/AMSR-E/AE_SI25.003 and https://doi.org/10.5067/TRUIAL3WPAUP; AMSR-E and AMSR2 SIC, https://doi.org/10.5067/AMSR-E/AE_SI25.003 and https://doi.org/10.5067/TRUIAL3WPAUP; AWI CS2SMOS, https://www.meereisportal.de; sea ice motion vectors, https://doi.org/10.5067/INAWUWO7QH7B; OIB, https://doi.org/10.5067/G519SHCKWQV6; CRREL IMB, http://imb-crrel-dartmouth.org; PIOMAS, http://psc.apl.uw.edu/research/projects/arctic-sea-ice-volume-anomaly; Kang et al., 2021, https://doi.org/10.1029/2020MS002448.
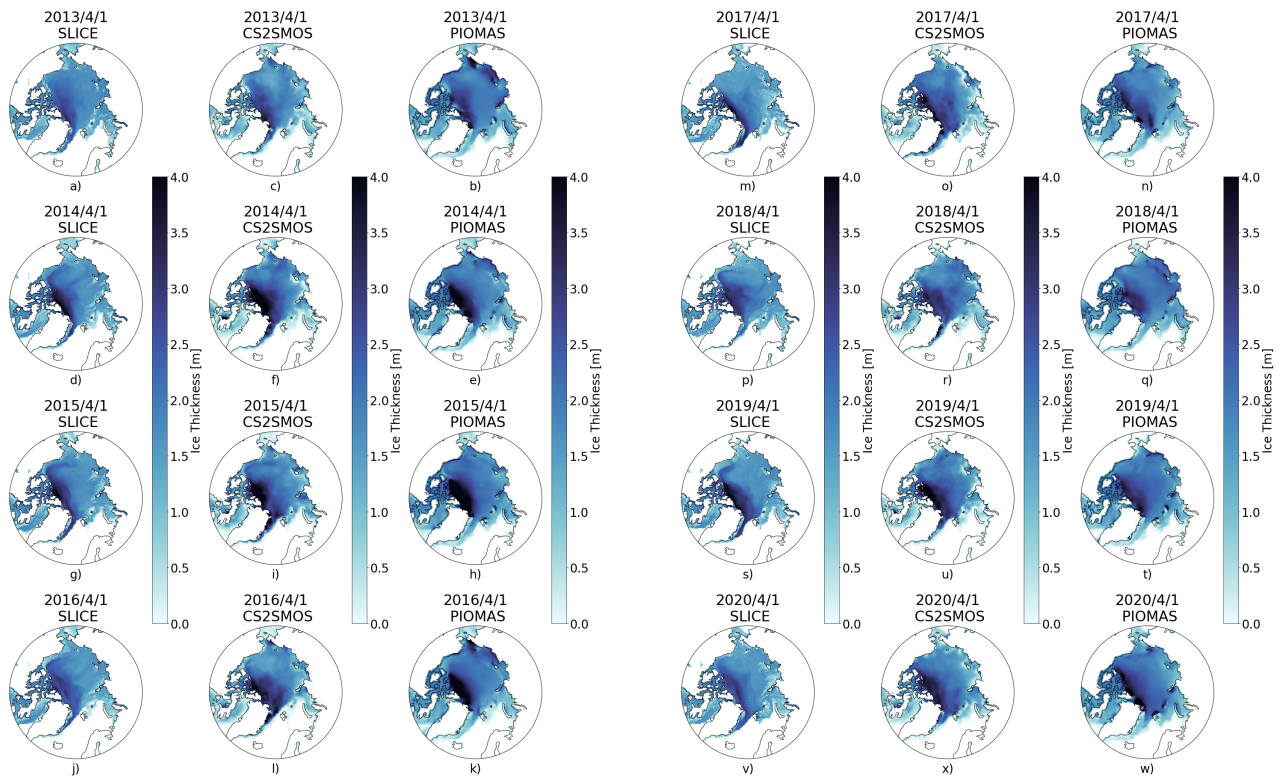
Figure A1. For the sea ice growth seasons ending in a–c) 2013, d–f) 2014, g–i) 2015, j–l) 2016, m–o) 2017, p–r) 2018, s–u) 2019 and v–x) 2020, a, d, g, j, m, p, s, v) SLICE sea ice thickness for 1 April, c, f, i, l, o, r, u, x) AWI CS2SMOS sea ice thickness from 1 April and b, e, h, k, n, q, t, w) PIOMAS sea ice thickness from 1 April.

Appendix A

495   *Author contributions.* All authors together conceived of the idea to use satellite retrieved snow–ice interface in a sea ice thickness satellite retrieval method. JA completed all analysis and wrote the first draft under guidance from YL and JK.

Competing interests. The authors declare that they have no conflict of interest.

Acknowledgements. This work was funded by the National Oceanic and Atmospheric Administration (NOAA) under grant no. NA20NES4320003. The views, opinions, and findings contained in this report are those of the author(s) and should not be construed as an official National Oceanic 500   and Atmospheric Administration or U.S. Government position, policy, or decision. The merging of CryoSat-2 und SMOS data was funded
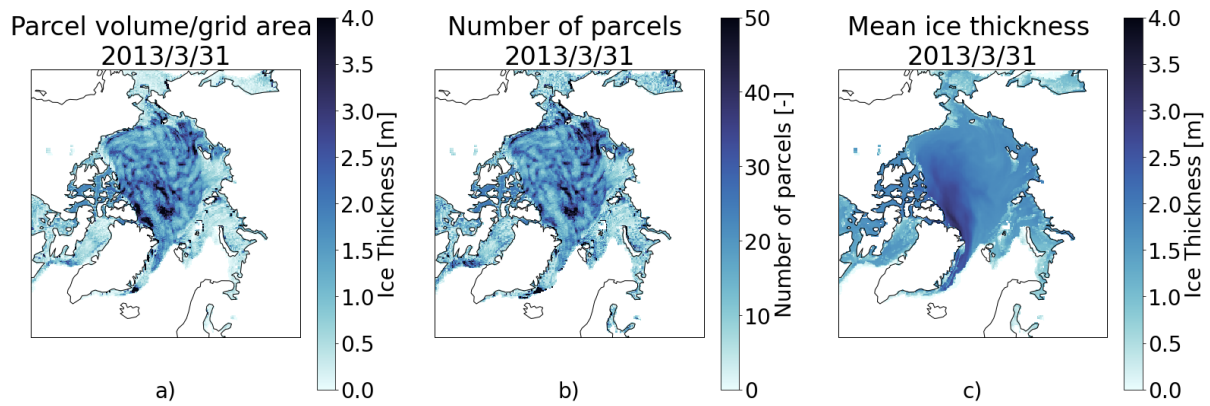
Figure A2. SLICE parcels on March 31 2013 (a) regridded using total parcel volume per grid cell divided by grid area, (b) counts within grid cell and (c) regridded mean parcel thickness within each grid cell. The volume per grid cell approach is unrealistic and dominated by erroneous convergence and divergence of parcels within grid cells.

by the ESA project SMOS & CryoSat-2 Sea Ice Data Product Processing and Dissemination Service and data from November 1st, 2012 to April 15th, 2021 were obtained from https://www.meereisportal.de (grant: REKLIM-2013-04).

References

Alexandrov, V., Sandven, S., Wahlin, J., , and Johannessen, O. M.: The relation between sea ice thickness and freeboard in the Arctic, Cryosphere, 4, 373–380, https://doi.org/10.5194/tc-4-373-2010, 2010.

Bailey, E., Feltham, D. L., and Sammonds, P. R.: A model for the consolidation of rafted sea ice, J. Geophys. Res.-Oceans, 115, C04 015, https://doi.org/10.1029/2008jc005103, 2010.

Batrak, Y., Kourzeneva, E., and Homleid, M.: Implementation of a simple thermodynamic sea ice scheme, SICE version 1.0-38h1, within the ALADIN-HIRLAM numerical weather prediction system version 38h1, Geoscientific Model Development, 11, 3347–3368, https://doi.org/10.5194/gmd-11-3347-2018, 2018.

Bitz, C. M. and Roe, G. H.: A mechanism for the high rate of sea ice thinning in the Arctic Ocean, J. Climate, 17, 3623–3632, https://doi.org/10.1175/1520-0442(2004)017<3623:amfthr>2.0.co;2, 2004.

Cavalieri, D. J., Gloersen, P., and Campbell, W. J.: Determination of sea ice parameters with the Nimbus-7 SMMR, J. Geophys. Res.-Atmos., 89, 5355–5369, https://doi.org/10.1029/JD089iD04p05355, 1984.

Cavalieri, D. J., Markus, T., and Comiso, J. C.: AMSR-E/Aqua Daily L3 25 km Brightness Temperature & Sea Ice Concentration Polar Grids, Version 3, Boulder, Colorado USA. NASA National Snow and Ice Data Center Distributed Active Archive Center [data set], https://doi.org/10.5067/AMSR-E/AE_SI25.003, 2014.

Comiso, J. C.: Sea ice effective microwave emissivities from satellite passive microwave and infrared observations, J. Geophys. Res.-Oceans, 88, 7686–7704, https://doi.org/10.1029/JC088iC12p07686, 1983.

Comiso, J. C.: Enhanced Sea Ice Concentrations and Ice Extents from AMSR-E Data, Journal of The Remote Sensing Society of Japan, 29, 199–215, https://doi.org/10.11440/rssj.29.199, 2009.

Connor, L. N., Laxon, S. W., Ridout, A. L., Krabill, W. B., and McAdoo, D. C.: Comparison of Envisat radar and airborne laser altimeter measurements over Arctic sea ice, Remote Sens. Environ., 113, 563–570, https://doi.org/10.1016/j.rse.2008.10.015, 2009.

Cox, G. F. N. and Weeks, W. F.: Numerical simulations of the profile properties of undeformed 1st-year sea ice during the growth season, Journal of Geophysical Research-Oceans, 93, 12 449–12 460, https://doi.org/10.1029/JC093iC10p12449, 1988.

DeRepentigny, P., Tremblay, L. B., Newton, R., and Pfirman, S.: Patterns of Sea Ice Retreat in the Transition to a Seasonally Ice-Free Arctic, J. Climate, 29, 6993 – 7008, https://doi.org/10.1175/JCLI-D-15-0733.1, 2016.

Docquier, D. and Koenigk, T.: Observation-based selection of climate models projects Arctic ice-free summers around 2035, Nature Communications Earth & Environment, 2, 144, https://doi.org/10.1038/s43247-021-00214-7, 2021.

Feltham, D. L., Untersteiner, N., Wettlaufer, J. S., and Worster, M. G.: Sea ice is a mushy layer, Geophysical Research Letters, 33, L14 501, https://doi.org/10.1029/2006gl026290, 2006.

Gloersen, P. and Cavalieri, D. J.: Reduction of weather effects in the calculation of sea ice concentration from microwave radiances, J. Geophys. Res.-Oceans, 91, 3913–3919, https://doi.org/10.1029/JC091iC03p03913, 1986.

Guerreiro, K., Fleury, S., Zakharova, E., Kouraev, A., Remy, F., and Maisongrande, P.: Comparison of CryoSat-2 and ENVISAT radar freeboard over Arctic sea ice: toward an improved Envisat freeboard retrieval, Cryosphere, 11, 2059–2073, https://doi.org/10.5194/tc-11-2059-2017, 2017.

Hall, D. K., Key, J. R., Casey, K. A., Riggs, G. A., and Cavalieri, D. J.: Sea ice surface temperature product from MODIS, IEEE T. Geosci. Remote., 42, 1076–1087, https://doi.org/10.1109/tgrs.2004.825587, 2004.

Hendricks, S. and Ricker, R.: Product User Guide & Algorithm Specification: AWI CryoSat-2 Sea Ice Thickness (version 2.3), https://doi.org/10013/epic.ecd56b5d-3e7d-4a65-9019-588b1c3b0d26, 2020.

Hendricks, S., Paul, S., and Rinne, E.: ESA Sea Ice Climate Change Initiative (Sea_Ice_cci): Northern hemisphere sea ice thickness from the CryoSat-2 satellite on a monthly grid (L3C), v2.0. Centre for Environmental Data Analysis, https://doi.org/10.5285/ff79d140824f42dd92b204b4f1e9e7c2, 2018.

Hersbach, H., Bell, B., Berrisford, P., Biavati, G., Horányi, A., Muñoz Sabater, J., Nicolas, J., Peubey, C., Radu, R.and Rozum, I., Schepers, D., Simmons, A., Soci, C., Dee, D., and Thépaut, J.-N.: ERA5 hourly data on pressure levels from 1979 to present, Copernicus Climate Change Service (C3S) Climate Data Store (CDS) [data set], https://doi.org/10.24381/cds.bd0915c6, 2018.

Hersbach, H., Bell, B., Berrisford, P., Hirahara, S., Horanyi, A., Munoz-Sabater, J., Nicolas, J., Peubey, C., Radu, R., Schepers, D., Simmons, A., Soci, C., Abdalla, S., Abellan, X., Balsamo, G., Bechtold, P., Biavati, G., Bidlot, J., Bonavita, M., De Chiara, G., Dahlgren, P., Dee, D., Diamantakis, M., Dragani, R., Flemming, J., Forbes, R., Fuentes, M., Geer, A., Haimberger, L., Healy, S., Hogan, R. J., Holm, E., Janiskova, M., Keeley, S., Laloyaux, P., Lopez, P., Lupu, C., Radnoti, G., de Rosnay, P., Rozum, I., Vamborg, F., Villaume, S., and Thepaut, J. N.: The ERA5 global reanalysis, Quarterly Journal of the Royal Meteorological Society, 146, 1999–2049, https://doi.org/10.1002/qj.3803, 2020.

Hewison, T. J. and English, S. J.: Airborne retrievals of snow and ice surface emissivity at millimeter wavelengths, IEEE T. Geosci. Remote., 37, 1871–1879, https://doi.org/10.1109/36.774700, 1999.

Hibler, W. D.: Dynamic Thermodynamic Sea Ice Model, J Phys. Oceanogr., 9, 815–846, https://doi.org/10.1175/1520-0485(1979)009<0815:adtsim>2.0.co;2, 1979.

Kang, E. J., Sohn, B. J., Tonboe, R. T., Dybkjaer, G., Holmlund, K., Kim, J. M., and Liu, C.: Implementation of a 1-D Thermodynamic Model for Simulating the Winter-Time Evolvement of Physical Properties of Snow and Ice Over the Arctic Ocean, J. Adv. Model. Earth Sy., 13, 3, https://doi.org/10.1029/2020ms002448, 2021.

Key, J., Wang, X. J., Liu, Y. H., Dworak, R., and Letterly, A.: The AVHRR Polar Pathfinder Climate Data Records, Remote Sensing, 8, 3, https://doi.org/10.3390/rs8030167, 2016.

Kilic, L., Tonboe, R. T., Prigent, C., and Heygster, G.: Estimating the snow depth, the snow–ice interface temperature, and the effective temperature of Arctic sea ice using Advanced Microwave Scanning Radiometer 2 and ice mass balance buoy data, Cryosphere, 13, 1283–1296, https://doi.org/10.5194/tc-13-1283-2019, 2019.

Krabill, W. B., Thomas, R. H., Martin, C. F., Swift, R. N., and Frederick, E. B.: Accuracy of airborne laser altimetry over the Greenland ice-sheet, International Journal of Remote Sensing, 16, 1211–1222, https://doi.org/10.1080/01431169508954472, 1995.

Kurtz, N., Studinger, M., Harbeck, J., Onana, V., and Yi., D.: IceBridge L4 Sea Ice Freeboard, Snow Depth, and Thickness, Version 1., Boulder, Colorado USA. NASA National Snow and Ice Data Center Distributed Active Archive Center [data set], https://doi.org/10.5067/G519SHCKWQV6, 2015.

Kurtz, N. T., Farrell, S. L., Studinger, M., Galin, N., Harbeck, J. P., Lindsay, R., Onana, V. D., Panzer, B., and Sonntag, J. G.: Sea ice thickness, freeboard, and snow depth products from Operation IceBridge airborne data, Cryosphere, 7, 1035–1056, https://doi.org/10.5194/tc-7-1035-2013, 2013.

Kurtz, N. T., Galin, N., and Studinger, M.: An improved CryoSat-2 sea ice freeboard retrieval algorithm through the use of waveform fitting, Cryosphere, 8, 1217–1237, https://doi.org/10.5194/tc-8-1217-2014, 2014a.

Kurtz, N. T., Galin, N., and Studinger, M.: An improved CryoSat-2 sea ice freeboard retrieval algorithm through the use of waveform fitting, Cryosphere, 8, 1217–1237, https://doi.org/10.5194/tc-8-1217-2014, 2014b.

Kwok, R. and Cunningham, G. F.: ICESat over Arctic sea ice: Estimation of snow depth and ice thickness, J. Geophys. Res.-Oceans, 113, C08 010, https://doi.org/10.1029/2008jc004753, 2008.

Kwok, R. and Cunningham, G. F.: Variability of Arctic sea ice thickness and volume from CryoSat-2, Philos. T. Roy. Soc. A, 373, 2045, https://doi.org/10.1098/rsta.2014.0157, 2015.

Kwok, R. and Rothrock, D. A.: Decline in Arctic sea ice thickness from submarine and ICESat records: 1958–2008, Geophys. Res. Lett., 36, https://doi.org/10.1029/2009GL039035, 2009.

Lavergne, T., Surensen, A. M., Kern, S., Tonboe, R., Notz, D., Aaboe, S., Bell, L., Dybkjaer, G., Eastwood, S., Gabarro, C., Heygster, G., Killie, M. A., Kreiner, M. B., Lavelle, J., Saldo, R., Sandven, S., and Pedersen, L. T.: Version 2 of the EUMETSAT OSI SAF and ESA CCI sea-ice concentration climate data records, Cryosphere, 13, 49–78, https://doi.org/10.5194/tc-13-49-2019, 2019.

Laxon, S. W., Giles, K. A., Ridout, A. L., Wingham, D. J., Willatt, R., Cullen, R., Kwok, R., Schweiger, A., Zhang, J. L., Haas, C., Hendricks, S., Krishfield, R., Kurtz, N., Farrell, S., and Davidson, M.: CryoSat-2 estimates of Arctic sea ice thickness and volume, Geophys. Res. Lett., 40, 732–737, https://doi.org/10.1002/grl.50193, 2013.

Lee, S. M. and Sohn, B. J.: Retrieving the refractive index, emissivity, and surface temperature of polar sea ice from 6.9GHz microwave measurements: A theoretical development, J. Geophys. Res.-Atmos., 120, 2293–2305, https://doi.org/10.1002/2014jd022481, 2015.

Lee, S. M., Sohn, B. J., and Kummerow, C. D.: Long-Term Arctic Snow/Ice Interface Temperature from Special Sensor for Microwave Imager Measurements, Remote Sensing, 10, 11, https://doi.org/10.3390/rs10111795, 2018.

Lei, R. B., Li, N., Heil, P., Cheng, B., Zhang, Z. H., and Sun, B.: Multiyear sea ice thermal regimes and oceanic heat flux derived from an ice mass balance buoy in the Arctic Ocean, Journal of Geophysical Research-Oceans, 119, 537–547, https://doi.org/10.1002/2012jc008731, 2014.

Lepparanta, M.: A Review of Analytical Models of Sea–Ice Growth, Atmos. Ocean, 31, 123–138, https://doi.org/10.1080/07055900.1993.9649465, 1993.

Liu, Y. H., Key, J. R., and Wang, X. J.: Influence of changes in sea ice concentration and cloud cover on recent Arctic surface temperature trends, Geophys. Res. Lett., 36, L20 710, https://doi.org/10.1029/2009gl040708, 2009.

Liu, Y. H., Key, J., and Mahoney, R.: Sea and Freshwater Ice Concentration from VIIRS on Suomi NPP and the Future JPSS Satellites, Remote Sensing, 8, 6, https://doi.org/10.3390/rs8060523, 2016.

Liu, Y. H., Key, J. R., Wang, X. J., and Tschudi, M.: Multidecadal Arctic sea ice thickness and volume derived from ice age, Cryosphere, 14, 1325–1345, https://doi.org/10.5194/tc-14-1325-2020, 2020.

Markus, T. and Cavalieri, D. J.: An enhancement of the NASA Team sea ice algorithm, IEEE T. Geosci. Remote., 38, 1387–1398, https://doi.org/10.1109/36.843033, 2000.

Markus, T. and Cavalieri, D. J.: The AMSR-E NT2 Sea Ice Concentration Algorithm : its Basis and Implementation, Journal of The Remote Sensing Society of Japan, 29, 216–225, https://doi.org/10.11440/rssj.29.216, 2009.

Markus, T., Neumann, T., Martino, A., Abdalati, W., Brunt, K., Csatho, B., Farrell, S., Fricker, H., Gardner, A., Harding, D., Jasinski, M., Kwok, R., Magruder, L., Lubin, D., Luthcke, S., Morison, J., Nelson, R., Neuenschwander, A., Palm, S., Popescu, S., Shum, C. K., Schutz, B. E., Smith, B., Yang, Y. K., and Zwally, J.: The Ice, Cloud, and land Elevation Satellite-2 (ICESat-2): Science requirements, concept, and implementation, Remote Sens. Environ., 190, 260–273, https://doi.org/10.1016/j.rse.2016.12.029, 2017.

Markus, T., Comiso, J. C., and Meier, W. N.: AMSR-E/AMSR2 Unified L3 Daily 25 km Brightness Temperatures & Sea Ice Concentration Polar Grids, Version 1, Boulder, Colorado USA. NASA National Snow and Ice Data Center Distributed Active Archive Center [data set], https://doi.org/10.5067/TRUIAL3WPAUP, 2018.

Massonnet, F., Vancoppenolle, M., Goosse, H., Docquier, D., Fichefet, T., and Blanchard-Wrigglesworth, E.: Arctic sea–ice change tied to its mean state through thermodynamic processes, Nat. Clim. Change, 8, 599–603, https://doi.org/10.1038/s41558-018-0204-z, 2018.

Mathew, N., Heygster, G., and Melsheimer, C.: Surface Emissivity of the Arctic Sea Ice at AMSR-E Frequencies, IEEE T. Geosci. Remote., 47, 4115–4124, https://doi.org/10.1109/tgrs.2009.2023667, 2009.

Mayer, M., Tietsche, S., Haimberger, L., Tsubouchi, T., Mayer, J., and Zuo, H.: An Improved Estimate of the Coupled Arctic Energy Budget, J. Climate, 32, 7915–7934, https://doi.org/10.1175/jcli-d-19-0233.1, 2019.

Maykut, G. A. and Untersteiner, N.: Some results from a time-dependent thermodynamic model of sea ice, Journal of Geophysical Research, 76, 1550–+, https://doi.org/10.1029/JC076i006p01550, 1971.

McPhee, M. G. and Untersteiner, N.: Using sea ice to measure vertical heat-flux in the ocean, Journal of Geophysical Research-Oceans, 87, 2071–2074, https://doi.org/10.1029/JC087iC03p02071, 1982.

Mecklenburg, S., Drusch, M., Kerr, Y. H., Font, J., Martin-Neira, M., Delwart, S., Buenadicha, G., Reul, N., Daganzo-Eusebio, E., Oliva, R., and Crapolicchio, R.: ESA's Soil Moisture and Ocean Salinity Mission: Mission Performance and Operations, IEEE T. Geosci. Remote., 50, 1354–1366, https://doi.org/10.1109/tgrs.2012.2187666, 2012.

Meier, W. N., Stewart, J. S., Liu, Y. H., Key, J., and Miller, J. A.: Operational Implementation of Sea Ice Concentration Estimates From the AMSR2 Sensor, IEEE J. Sel. Top. Appl., 10, 3904–3911, https://doi.org/10.1109/jstars.2017.2693120, 2017.

Notz, D.: Thermodynamic and fluid-dynamical processes in sea ice, Ph.D. thesis, Cambridge University, 2005.

Panzer, B., Gomez-Garcia, D., Leuschen, C., Paden, J., Rodriguez-Morales, F., Patel, A., Markus, T., Holt, B., and Gogineni, P.: An ultra-wideband, microwave radar for measuring snow thickness on sea ice and mapping near-surface internal layers in polar firn, Journal of Glaciology, 59, 244–254, https://doi.org/10.3189/2013JoG12J128, 2013.

Perovich, D., Richter-Menge, J., and Polashenski, C.: Observing and understanding climate change: Monitoring the mass balance, motion, and thickness of Arctic sea ice, http://imb-crrel-dartmouth.org, 2021.

Perovich, D. K. and Elder, B.: Estimates of ocean heat flux at SHEBA, Geophysical Research Letters, 29, https://doi.org/10.1029/2001gl014171, 2002.

Petty, A. A., Kurtz, N. T., Kwok, R., Markus, T., and Neumann, T. A.: Winter Arctic sea ice thickness from ICESat-2 freeboards, Journal of Geophysical Research-Oceans, 125, https://doi.org/10.1029/2019JC015764, 2020.

Polashenski, C., Perovich, D., Richter-Menge, J., and Elder, B.: Seasonal ice mass-balance buoys: adapting tools to the changing Arctic, Ann. Glaciol., 52, 18–26, https://doi.org/10.3189/172756411795931516, 2011.

Richter-Menge, J. A., Perovich, D. K., Elder, B. C., Claffey, K., Rigor, I., and Ortmeyer, M.: Ice mass–balance buoys: a tool for measuring and attributing changes in the thickness of the Arctic sea–ice cover, Ann. Glaciol., 44, 205–210, https://doi.org/10.3189/172756406781811727, 2006.

Ricker, R., Hendricks, S., Helm, V., Skourup, H., and Davidson, M.: Sensitivity of CryoSat-2 Arctic sea–ice freeboard and thickness on radar-waveform interpretation, Cryosphere, 8, 1607–1622, https://doi.org/10.5194/tc-8-1607-2014, 2014.

Ricker, R., Hendricks, S., Kaleschke, L., and Tian-Kunze, X.: CS2SMOS User Guide v3.0, https://doi.org/10013/epic.51136, 2017a.

Ricker, R., Hendricks, S., Kaleschke, L., Tian-Kunze, X., King, J., and Haas, C.: A weekly Arctic sea-ice thickness data record from merged CryoSat-2 and SMOS satellite data, Cryosphere, 11, 1607–1623, https://doi.org/10.5194/tc-11-1607-2017, 2017b.

Sallila, H., Farrell, S. L., McCurry, J., and Rinne, E.: Assessment of contemporary satellite sea ice thickness products for Arctic sea ice, Cryosphere, 13, 1187–1213, https://doi.org/10.5194/tc-13-1187-2019, 2019.

Saunders, R., Hocking, J., Turner, E., Rayer, P., Rundle, D., Brunel, P., Vidot, J., Roquet, P., Matricardi, M., Geer, A., Bormann, N., and Lupu, C.: An update on the RTTOV fast radiative transfer model (currently at version 12), Geoscientific Model Development, 11, 2717–2732, https://doi.org/10.5194/gmd-11-2717-2018, 2018.

655 Schweiger, A., Lindsay, R., Zhang, J. L., Steele, M., Stern, H., and Kwok, R.: Uncertainty in modeled Arctic sea ice volume, J. Geophys. Res.-Oceans, 116, C00D06, https://doi.org/10.1029/2011jc007084, 2011.

Schwerdtfecer, P.: The Thermal Properties of Sea Ice, Journal of Glaciology, 4, 789–807, https://doi.org/10.3189/S0022143000028379, 1963.

Screen, J. A. and Simmonds, I.: The central role of diminishing sea ice in recent Arctic temperature amplification, Nature, 464, 1334–1337, https://doi.org/10.1038/nature09051, 2010.

660 Sohn, B. J. and Lee, S. M.: Analytical relationship between polarized reflectivities on the specular surface, Int. J. Remote Sens., 34, 2368–2374, https://doi.org/10.1080/01431161.2012.744490, 2013.

Stefan, J.: Ueber die Theorie der Eisbildung, insbesondere über die Eisbildung im Polarmeere, Ann. der Phy.-Berlin, 278, 269–286, https://doi.org/https://doi.org/10.1002/andp.18912780206, 1891.

Stroeve, J. C., Serreze, M. C., Holland, M. M., Kay, J. E., Malanik, J., and Barrett, A. P.: The Arctic's rapidly shrinking sea ice cover: a
665 research synthesis, Climatic Change, 110, 1005–1027, https://doi.org/10.1007/s10584-011-0101-1, 2012.

Thorndike, A. S., Rothrock, D. A., Maykut, G. A., and Colony, R.: Thickness Distribution of Sea Ice, J. Geophys. Res.-Oc. Atm., 80, 4501–4513, https://doi.org/10.1029/JC080i033p04501, 1975.

Tian-Kunze, X., Kaleschke, L., Maass, N., Makynen, M., Serra, N., Drusch, M., and Krumpen, T.: SMOS-derived thin sea ice thickness: algorithm baseline, product specifications and initial verification, Cryosphere, 8, 997–1018, https://doi.org/10.5194/tc-8-997-2014, 2014.

670 Tilling, R. L., Ridout, A., and Shepherd, A.: Estimating Arctic sea ice thickness and volume using CryoSat-2 radar altimeter data, Adv. Space Res., 62, 1203–1225, https://doi.org/10.1016/j.asr.2017.10.051, 2018.

Tschudi, M., Meier, W. N., Stewart, J. S., Fowler, C., and Maslanik, J.: Polar Pathfinder Daily 25 km EASE-Grid Sea Ice Motion Vectors, Version 4, Boulder, Colorado USA. NASA National Snow and Ice Data Center Distributed Active Archive Center [data set], https://doi.org/10.5067/INAWUWO7QH7B, 2019.

675 Tschudi, M. A., Meier, W. N., and Stewart, J. S.: An enhancement to sea ice motion and age products at the National Snow and Ice Data Center (NSIDC), Cryosphere, 14, 1519–1536, https://doi.org/10.5194/tc-14-1519-2020, 2020.

Wang, X. J., Key, J., Kwok, R., and Zhang, J. L.: Comparison of Arctic Sea Ice Thickness from Satellites, Aircraft, and PIOMAS Data, Remote Sensing, 8, 9, https://doi.org/10.3390/rs8090713, 2016.

Wingham, D. J., Francis, C. R., Baker, S., Bouzinac, C., Brockley, D., Cullen, R., de Chateau-Thierry, P., Laxon, S. W., Mallow, U.,
680 Mavrocordatos, C., Phalippou, L., Ratier, G., Rey, L., Rostan, F., Viau, P., and Wallis, D. W.: CryoSat: A mission to determine the fluctuations in Earth's land and marine ice fields, Natural Hazards and Oceanographic Processes from Satellite Data, 37, 841–871, https://doi.org/10.1016/j.asr.2005.07.027, 2006.

Zhang, J. L. and Rothrock, D. A.: Modeling global sea ice with a thickness and enthalpy distribution model in generalized curvilinear coordinates, Mon. Weather Rev., 131, 845–861, https://doi.org/10.1175/1520-0493(2003)131<0845:mgsiwa>2.0.co;2, 2003.